Review

# Using high-resolution quantitative mapping of R1 as an index of cortical myelination

Antoine Lutti [a,b,*], Frederic Dick [c,d], Martin I. Sereno [c,d,e], Nikolaus Weiskopf [a]

[a] Wellcome Trust Centre for Neuroimaging, UCL Institute of Neurology, University College London, London, UK
[b] LREN, Département des neurosciences cliniques, CHUV, University of Lausanne, Lausanne, Switzerland
[c] Birkbeck/UCL Centre for NeuroImaging, London, UK
[d] Department of Psychological Sciences, Birkbeck College, University of London, UK
[e] Perceptual and Language Sciences Division, UCL, London, UK

## ARTICLE INFO

## ABSTRACT

A fundamental tenet of neuroscience is that cortical functional differentiation is related to the cross-areal differences in cyto-, receptor-, and myeloarchitectonics that are observed in ex-vivo preparations. An ongoing challenge is to create noninvasive magnetic resonance (MR) imaging techniques that offer sufficient resolution, tissue contrast, accuracy and precision to allow for characterization of cortical architecture over an entire living human brain. One exciting development is the advent of fast, high-resolution *quantitative* mapping of basic MR parameters that reflect cortical myeloarchitecture. Here, we outline some of the theoretical and technical advances underlying this technique, particularly in terms of measuring and correcting for transmit and receive radio frequency field inhomogeneities. We also discuss new directions in analytic techniques, including higher resolution reconstructions of the cortical surface. We then discuss two recent applications of this technique. The first compares individual and group myelin maps to functional retinotopic maps in the same individuals, demonstrating a close relationship between functionally and myeloarchitectonically defined areal boundaries (as well as revealing an interesting disparity in a highly studied visual area). The second combines tonotopic and myeloarchitectonic mapping to localize primary auditory areas in individual healthy adults, using a similar strategy as combined electrophysiological and post-mortem myeloarchitectonic studies in non-human primates.

© 2013 Elsevier Inc. All rights reserved.

## Contents

* Corresponding author at: Wellcome Trust Centre for Neuroimaging, UCL Institute of Neurology, University College London, London, UK.
  E-mail addresses: a.lutti@ucl.ac.uk, antoinelutti@gmail.com (A. Lutti).

## Introduction

A basic goal in neuroscience is to map out the functional landscape of cerebral cortical areas identified by structural characteristics (cyto- and myeloarchitecture — Clarke and Miklossy, 1990; Flechsig, 1920; Förster, 1934; Hopf, 1951, 1955; Smith, 1907; Vogt, 1906; von Economo and Koskinas, 1925), response preferences, or sensory or motor mapping (Zilles and Amunts, 2010). Identifying homologous areas across species helps us understand how areal function itself has evolved (cf., reptilian jaw bones evolving into inner ear ossicles in mammals). In humans, in-vivo identification of cortical areas generally relies on fMRI mapping of representations of the sensory surfaces (e.g., retinotopy/cochleotopy/somatotopy), motor effectors, or higher level equivalents (attention-o-topy, intention-o-topy). This has been an extremely productive approach, and has shown that much of the cortex is tiled with maps (Graziano and Aflalo, 2007; Schreiner and Winer, 2007; Wandell et al., 2007). These maps not only tend to have a generally consistent location and orientation on the cortical sheet, but also show non-trivial individual differences in size, shape, and possibly even neighbor relations (Sereno and Tootell, 2005) that may have interesting functional consequences (Schwarzkopf et al., 2011).

However, identifying cortical areas through sensory and motor mapping is time consuming; it takes an hour to accurately map one modality (e.g., polar angle and eccentricity mapping to establish visual areas). The robustness, reliability, and extent of maps are strongly dependent upon the participant's level of directed attention to the stimulus over this long period of scanning (Saygin and Sereno, 2008; Silver and Kastner, 2009) making mapping more difficult in children, elderly, and clinical populations. Some cortical areas cannot be defined on the basis of functional maps alone (e.g., primary auditory areas A1 & R — (Dick et al., 2012; Hackett, 2011). And in some individuals (e.g., auditory areas in the deaf (Karns et al., 2012; Ressel et al., 2012), visual areas in the blind, and somatomotor areas in participants with hemiparesis, deafferentation, or amputations), defining inputs or outputs may be absent.

One means of estimating an individual participant's cortical areas is by probabilistic, postmortem cytoarchitectonic atlases, which are provided in a standard anatomical MRI volume or MRI-based cortical surface space (through affine or non-linear transformations (Eickhoff et al., 2005; Fischl et al., 1999; Tahmasebi et al., 2009)). This requires no additional scanning time, can define a large number of cortical areas at once (12 Brodmann areas are defined in the current Freesurfer distribution), and facilitates easy comparisons across experiments, scanner sites, and labs. Unfortunately, the degree of inter-individual variation in areal size and shape is considerable (with three-fold areal differences even in V1 — (Schwarzkopf et al., 2011)), making precise definition of any area – particularly smaller and more variable ones – very challenging. This is of particular concern when localizing areas for surgical implantation (e.g., neurostimulators, drug delivery vehicles, or electrode recording grids) or excision (e.g., temporal lobectomy).

A better solution would be to use the signal and tissue contrast information in the MRI anatomical volume itself to identify an individual participant's cortical areas. Indeed, over the last decade much progress has been made in mapping individual cortical areas in-vivo by taking advantage of the sensitivity of the MR longitudinal relaxation time T1 to myelin content, an in-vivo assay of myeloarchitecture (Barazany and Assaf, 2012; Bock et al., 2009, 2013; Clark et al., 1992; Dick et al., 2012; Geyer et al., 2011; Glasser and Van Essen, 2011; Sánchez-Panchuelo et al., 2012; Sereno et al., in press; Sigalovsky et al., 2006; Walters et al., 2003). These myelin mapping methods use different combinations of high resolution images, including high-resolution proton-density (Clark et al., 1992), T1-weighted images (Barazany and Assaf, 2012; Walters et al., 2003), T2-weighted images (Trampel et al., 2011) and volumes derived by taking a ratio of T1- and T2-weighted volumes (Glasser and Van Essen, 2011), synthetic, high-contrast images derived from multi-angle FLASH (Hinds et al., 2008),

and quantitative R1 (1/T1) images (Dick et al., 2012; Sereno et al., in press; Sigalovsky et al., 2006).

The recent achievements illustrating the advent of in-vivo histological studies are notable given the technical challenges posed. First, the degree of cortical myelination is strongly cortical-layer-dependent (for examples, see Annese et al., 2004; Braitenberg, 1962). Thus, MRI scans must be of sufficiently high resolution to resolve laminar differences to some degree. Second, interareal differences in myelination are comparable in magnitude to the differences in myelination across layers; upper layers of cortex are often quite lightly myelinated (see whole-brain-slice Gallyas stain of macaque, shown in Fig. 2 of Bridge et al., 2014). Therefore, even minor local inaccuracies in cortical surface reconstruction can significantly distort or obscure estimates of areal differences in myelination. Third, because of the subtlety of the cross-areal differences in myelination, even fairly gentle spatial biases in overall signal intensity and contrast can swamp myelin-related signal changes. In particular, transmit-field (B1+) inhomogeneities affect image contrast and can bedevil widely applied post-hoc histogram-based normalization methods (e.g. Dale et al., 1999) and also ratio methods based on normalizing scans (Glasser and Van Essen, 2011). Myelin mapping methods that combine different kinds of scans must also often contend with vessel artifacts and local spatial distortion that differ between scan types. (However, such ratio-based methods have the advantage of potentially broader application as they rely on widely-available clinical pulse sequences).

In addition to the need for high resolution and spatially unbiased data for myelin mapping, it would be very useful to be able to measure differences in myelination in the same area either over different subjects, or over time in the same subject. However this is not possible with cortical myelination measurements derived from post-hoc normalized contrast-weighted images or from image ratios, in that their numerical values are inherently arbitrary, and unstable even on a single scanner. The ability to make quantitative cross-scan, cross-individual, and cross-site comparisons of cortical myelination would allow for the establishment of norms across development, populations and disease stages (e.g., in multiple sclerosis, Alzheimer's disease and focal dystonias).

To address these challenges, we have developed and refined a method for measuring cortical myelination that takes advantage of recent advances in high-resolution, quantitative MR imaging. Here, we first lay out in some detail the underlying theory and recent advances in MR physics that made high resolution quantitative imaging possible, and discuss the advantages and drawbacks of different quantitative imaging schemes. We then present results from several initial studies using these techniques to measure cortical myelination in visual (Sereno et al., in press) and auditory areas (Dick et al., 2012).

## Myelin mapping using R1 mapping methods

T1 is the time constant governing the recovery of the longitudinal component of the magnetization following radio-frequency (RF) excitation, and crucially, an MR parameter closely related to tissue myelination (Koenig et al., 1990) and in particular, the cholesterol that is bound to myelin (Koenig, 1991). Ex-vivo studies using white matter slices from patients with multiple sclerosis or controls have directly compared quantitative MRI measurements of these slices with microscopic histology-based estimates of their regional myelin content. T1 relaxation times are highly correlated with myelin content in unfixed spinal cord (r = 0.78, Mottershead et al., 2003), unfixed brain (r = 0.70, Schmierer et al., 2004; r = 0.77, Schmierer et al., 2008), and fixed brain (r = 0.89, Schmierer et al., 2008). To our knowledge, there are no combined quantitative MR and quantitative histology studies directly assessing the T1/myelin correlation in cortical gray matter, but there is no a priori reason to expect this relationship to be different.

Signal equations establish the relationship between the signal acquired using a given MR pulse sequence and the MR parameters of the imaged object. In quantitative MRI (qMRI), these equations are inverted in order to yield quantitative estimates of the MR parameters (e.g. T1, Proton Density (PD), apparent transverse relaxation time T2*, and so on), which are indicative of the underlying tissue microarchitecture. As a general rule, quantitative mapping requires a number of acquired datasets at least equal to the number of MR parameters to quantify (the unknowns in the signal equations). Because the acquired signal is a mixed effect of multiple MR parameters and systematic bias in the MR parameter estimates is often present, qMRI can require a large number of acquired datasets. Therefore, a significant challenge for quantitative mapping is efficiency, i.e. quantification of MR parameters from the minimum possible number of datasets. The time saved by reducing the number of datasets can be used instead to optimize the precision of the quantitative maps and/ or to quantitatively map multiple MR parameters (Helms et al., 2008a,b). This is particularly relevant for high-resolution applications where acquisition times are long and averaging may help maximize the signal-to-noise ratio.

Another criterion of paramount importance for qMRI is accuracy. As noted in the Introduction section, the systematic bias present in MRI data (Helms et al., 2008a; Yarnykh, 2010) can be many times larger than the subtle changes in MR signal due to myelin variation (~1% in R1 scans, see Dick et al., 2012; Sereno et al., in press). Therefore, such bias must be accurately corrected to obtain quantitative MR parameter estimates of tissue microarchitecture. Systematic bias may affect any type of MR acquisition but is generally overlooked in standard T1-weighted anatomical imaging, only allowing a qualitative phenomenological description of brain morphology. For instance, a typical high-resolution MPRAGE scan at 1.5 T can show 50% variation in signal intensity over homologous regions in the left and right hemispheres. In contrast, estimation of tissue myelination by quantitative MR techniques demands particular attention to bias correction.

Several quantitative MRI methods exist that yield biomarkers reflective of tissue myelination e.g. Magnetization Transfer (MT) mapping (Henkelman et al., 1993) and Myelin Water Fraction mapping (MacKay et al., 2006). It is not the goal of this review to discuss and compare the different quantitative MRI methods that might be applicable to the detection of cortical myelination. Rather, we limit ourselves to the discussion of the methodological developments that have enabled the recent detection of cortical myelination variations using R1 mapping.

*Quantitative R1 (1/T1) mapping*

R1 ($= 1 / T1$) is often mapped, as the image intensity then corresponds to the more familiar tissue contrast of T1-weighted images and R1 can most easily be related to tissue microarchitecture (Rooney et al., 2007). A number of existing methods for measuring R1 monitor the recovery of the longitudinal magnetization after a full inversion pulse. Because high-resolution images cannot be obtained from a single inversion without a significant degradation in image quality, several repetitions of the inversion recovery are required. To ensure consistency across repetitions, full recovery of the longitudinal component must be achieved between the inversions, making the total scan time prohibitively long for in-vivo applications.

The Look–Locker technique improves the efficiency of inversion–recovery methods by acquiring multiple sample points after each inversion (Look and Locker, 1970). When a dense sampling of the T1 recovery is desirable, the same image encoding may be used for all sample points of a given inversion (Gowland and Leach, 1992). The long resulting scan time only allows for single-slice acquisitions in-vivo. We focus here on methods for whole brain R1 mapping based on only a few points along the recovery curve. Look–Locker was originally combined with snapshot-FLASH readouts (Deichmann and Haase, 1992;

Haase, 1990; Haase et al., 1989) and EPI readouts (Freeman et al., 1998; Gowland and Mansfield, 1993; Ordidge et al., 1990). Inversion–recovery methods based on EPI readouts are generally faster but suffer from susceptibility-induced effects that affect image quality. Segmented acquisitions optimize acquisition speed with minimal effect on image quality (Lee, 2000). The delay for T1 recovery in a given slice may be used to sample the inversion recovery in neighboring slices, leading to significant improvements in imaging speed (Clare and Jezzard, 2001; Deichmann, 2005; Zhu and Penn, 2005).

Magnetization saturation was introduced to minimize this delay time, further reducing the acquisition time (Deichmann et al., 1999). Magnetization saturation has been combined with sequential slice and segmented k-space acquisitions to achieve a high sampling of the recovery curve in a minimal acquisition time (Shah et al., 2001; Steinhoff et al., 2001). Note that sub-optimal inversion efficiency and inhomogeneous excitation through 2D slices might induce a bias that requires calibration (Deichmann, 2005). Also, imperfect slice profiles yield deviations from the nominal slice thickness.

The use of non-selective RF pulses and of 3D image encoding schemes helps minimize these issues encountered in 2D imaging. 3D acquisitions are also preferable for high-resolution R1 mapping as they yield higher image SNR than their 2D counterparts. A segmented acquisition was introduced by Henderson et al. (1999) for rapid R1 mapping in three dimensions based on the Look–Locker principle. It should be noted that inhomogeneities in RF excitation induce a bias in the R1 estimates provided by the Look–Locker technique. This can be corrected using maps of flip angle distributions obtained from specifically dedicated MRI acquisitions (see below). Alternatively the true relaxation rate might be obtained from a three-point fit of the relaxation curve, at the cost of an increased acquisition time (Deichmann, 2005; Steinhoff et al., 2001).

Alternative approaches with reduced sensitivity to RF inhomogeneities were developed based on MPRAGE acquisitions (Mugler and Brookeman, 1990). Marques et al. (2010) extracted quantitative R1 maps from the ratio of two MPRAGE images acquired with different excitation flip angles and inversion times — a technique called MP2RAGE. The resulting R1 maps were corrected for the effects of the RF receive field $B_1^-$ and of R2*. Inhomogeneous excitation effects were minimized using optimal acquisition settings but some bias remained in the R1 maps. Despite this, the MP2RAGE technique has been used to detect the subtle variations in myelination across the cortex (Marques and Gruetter, 2013; Tardif et al., 2013; Waehnert et al., 2013, 2014; Weiss et al., 2011).

The method developed by Liu et al. (2011) yields R1 maps insensitive to RF inhomogeneities due to the use of three inversion times. The resulting increase in scan time and the handling of complex raw data required for calculation of the R1 maps might represent significant practical limitations for this method. T1-weighted images based on MPRAGE acquisitions have also been designed to yield optimal contrast within the cortical layer (Bock et al., 2013). However some effects from inhomogeneous RF excitation remain in the data and the total acquisition time might be prohibitive for high-resolution whole brain imaging. This method also does not yield fully quantitative R1 maps, which limits the insight into tissue microarchitecture.

Variable flip-angle (VFA) methods calculate R1 from the signal change between datasets acquired with different nominal flip angles of the RF excitation (Sigalovsky et al., 2006). 3D spoiled gradient-echo schemes ('FLASH', 'SPGR' or 'FFE') are generally preferred for image encoding due to their high time-efficiency and the reduced contribution of other MR parameters (e.g. T2*) to the detected signal (Haase et al., 1986; Homer and Beevers, 1985; Homer and Roberts, 1987). With VFA methods, whole-brain 1 mm$^3$ resolution quantitative R1 maps can be obtained in under 8 min using two nominal flip angle values (Deoni et al., 2003; Wang et al., 1987). If time allows, a larger number of nominal flip angle values may be used to improve accuracy and precision (Sigalovsky et al., 2006).

A significant challenge with VFA methods is their sensitivity to the spatially inhomogeneous RF transmit excitation field B1+, which arises from the increased coupling between the RF transmit field and the human head at high field strength (Glover et al., 1985). RF inhomogeneities lead to a distribution of excitation flip angles throughout the brain, i.e. to deviations between the local (true) and nominal (prescribed) flip angle values. If RF inhomogeneities are present, the use of the nominal flip angle values in the signal equation leads to systematic bias in the R1 estimates as shown in Fig. 1a. This bias clearly resembles the pattern of RF inhomogeneities shown in Fig. 1b. Because R1 is proportional to the square of the flip angle values for VFA methods (Helms et al., 2008a), the ±25% variations of the local (true) flip angle at 3 T impose a ~50% bias on the R1 maps (Weiskopf et al., 2011), much larger than the ~1% changes in R1 due to variation in myelination levels (Dick et al., 2012; Sereno et al., in press). This bias is removed from the R1 maps when the correct local flip angle values are used in the R1 estimation based on the signal equations (see Fig. 1c). As we describe in the next section, local flip angle values can be obtained by accurate mapping of the RF transmit field B1+.

*B1+ mapping*

To avoid any systematic bias of the measured B1+ values due to residual dependence on R1, independent mapping of the B1+ inhomogeneities using a separate method might be preferred (Venkatesan et al., 1998). A variety of B1+ mapping methods have been proposed (Akoka et al., 1993; Helms et al., 2008c; Insko and Bolinger, 1993; Jiru and Klose, 2006; Sacolick et al., 2010; Sled and Pike, 1998, 2000; Wang et al., 2005; Yarnykh, 2007) and some of them systematically compared (Lutti et al., 2010). Slice-selective RF pulses are generally avoided as they lead to systematic bias of the B1+ maps which must be accurately corrected (Helms et al., 2008c; Hsu et al., 2009). Off-resonance precession effects impose a systematic bias which increases with field strength, but can be minimized by the use of RF pulses with maximal amplitudes (Fleysher et al., 2011; Lutti et al., 2012).

A large fraction of the existing methods estimate the B1+ distributions from the signal change across several nominal RF flip angle values (Akoka et al., 1993; Insko and Bolinger, 1993; Sled and Pike, 1998, 2000; Wang et al., 2005). However as was observed in the context of R1 mapping, the R1-dependence of the signal change may bias the B1+ estimates. Long repetition times (TR ≥ 5T1) avoid this bias but lead to long acquisition times that are prohibitive in-vivo. Minimization of the R1 bias in the B1+ maps at no cost in acquisition

time can be implemented using 'resetting' pulses (Cunningham et al., 2006; Stollberger and Wach, 1996) or by using ratio of images acquired during the same repetitions (Akoka et al., 1993; Jiru and Klose, 2006; Lutti et al., 2010, 2012).

The actual flip-angle imaging (AFI) method proposed by Yarnykh (2007) is an attractive alternative since the independence of the resulting B1+ maps on R1 allows the use of short TRs and therefore short acquisitions. However the strong gradient spoiling required to ensure appropriate spoiling of transverse coherences imposes a limit on the minimum achievable acquisition time (Nehrke, 2009; Yarnykh, 2010). The STEAM method recently proposed by Nehrke and Börnert (2012) might be an interesting option when B1+ maps with minimal T1-bias must be calculated from ultra-fast acquisition to minimize scan time.

Alternative methods exist that calculate B1+ distributions based on the phase information of MRI images. Phase-based approaches have clear advantages over conventional methods based on magnitude data. These include independence of the B1+ estimates from the R1 values as well as a wider dynamic range, which is beneficial when the local RF flip angles are small (Morrell, 2008). The method proposed by Sacolick et al. (2010) based on the Bloch–Siegert shift offers also the possibility of using short TR values, thereby reducing acquisition time. Note that novel types of off-resonance RF pulses have been designed to mitigate the Specific Absorption Rate (SAR) problems of the Bloch–Siegert method at ultra-high field (Jankiewicz et al., 2013).

Few methods have demonstrated the level of accuracy and efficiency required for whole-brain in-vivo myelin mapping using quantitative mapping. In particular the challenge of large B1+ inhomogeneities at high field strengths requires methods with a large dynamic range. This can be successfully achieved by acquisition of data over a large range of nominal RF flip angle values, ensuring optimal B1+ calculation at each voxel location and yielding whole brain B1+ maps with a very high level of accuracy even at ultra-high field (Lutti et al., 2012). Parallel imaging can be used to keep the total acquisition time below 5 min, as is required from a reference scan whose sole purpose is the bias correction of R1 maps (Lutti et al., 2012). Image distortions resulting from the EPI readouts used with this method are minimized using a short readout duration, achieved thanks to the small matrix size and use of parallel imaging along the phase-encode direction. The remaining geometric distortions are corrected at the post-processing stage using a well-established procedure extensively used for fMRI acquisitions (Hutton et al., 2002; Lutti et al., 2010). This method has been shown to produce accurate and precise B1+ maps over the whole brain even at 7 T (Lutti et al., 2012).
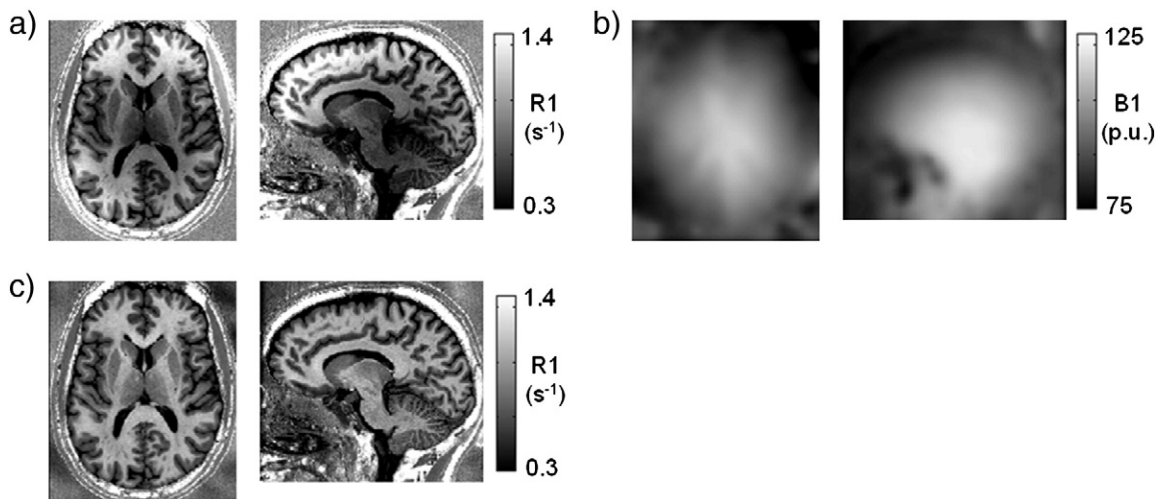


Fig. 1. Effects of RF transmit field (B1+) inhomogeneities on estimates of R1: a) R1 volume, calculated using nominal flip angle values in Bloch equations; b) B1+ map of same subject, showing ±25% inhomogeneities in flip angle, which translate into the ~50% biases in R1 seen in a, c) corrected R1 volume, calculated using local flip angle derived from B1+ map.

Optimization of the dynamic range with variable RF flip angles could be implemented with the method presented by Chung et al. (2010), based on signal acquisition following a preconditioning RF pulse of variable nominal value. Alternatively, the SA2RAGE sequence (Eggenschwiler et al., 2012) has been optimized to accurately map the B1+ distributions over a large range of local flip angles in a minimal acquisition time. This method also keeps SAR levels at low values and might be a particularly suitable option for ultra-high field applications. Alternatively, the original AFI method can be extended to address the issue of increased B1+ inhomogeneities at high field (Fleysher et al., 2011).

*Combined R1 and B1+ mapping*

A number of methods have emerged over the recent years for combined estimation of the B1+ and T1 distributions from the same type of MR readout. The main motivation for this combined approach is to improve the consistency of the theoretical modeling and of the datasets used for quantitative imaging. The DESPOT1-HIFI (Deoni, 2007), VAFI (Hurley et al., 2012), TriTone (Fleysher et al., 2008), MTM (Voigt et al., 2010) and MoS (Chavez and Stanisz, 2012) methods combine the estimation of the B1+ and T1 values using the type of MR acquisitions (FLASH/SPGR) used for VFA methods. In the DESPOT1-HIFI method (Deoni, 2007), the VFA acquisition is complemented by an extra acquisition where an inversion pulse is played out prior to the FLASH/SPGR readout. The lower accuracy of the resulting R1 maps in tissues with long TRs might be improved with an extra acquisition. The TriTone (Fleysher et al., 2008) method uses three VFA acquisitions and calculation of the T1 values is completed by the removal of B1+ inhomogeneity effects at post-processing.

The MTM technique (Voigt et al., 2010) is an extension of the original AFI method for B1+ mapping (Yarnykh, 2007) where data are acquired over multiple TR values; compared to the original AFI instantiation, significant improvements in B1+ accuracy and reproducibility were found. A somewhat similar approach is the VAFI method (Hurley et al., 2012), which combines one VFA run with an AFI acquisition originally designed for B1+ mapping (Yarnykh, 2007). The faster combined VAFI method proved more robust than acquiring and analyzing VFA and AFI runs separately (Hurley et al., 2012). Finally, the MoS method (Chavez and Stanisz, 2012) extracts B1+ and T1 estimates from the linearization of the FLASH/SPGR signal equations at high and low flip angles. The artifactual coupling between the apparent B1+ and T1 values where the RF transmit field is low illustrates the difficulty in extracting independent B1+ and T1 estimates. An interesting alternative is the method proposed by Hsu et al. (2009) which concurrently estimates B1+ and R1 from the subtraction of MRI signals acquired with different flip angles and sequence timings.

## Beyond R1 mapping — challenges for quantitative mapping techniques

Large discrepancies exist between R1 estimates obtained from different methods (Cheng and Wright, 2006; Clare and Jezzard, 2001; Deoni, 2007; Deoni et al., 2005; Ethofer et al., 2003; Gelman et al., 2001; Preibisch and Deichmann, 2009; Wansapura et al., 1999; Wright et al., 2008; Zhu and Penn, 2005). Such differences might in part be due to imperfect correction of B1+-inhomogeneities (as noted above), partial volume effects between different tissue types at low image resolutions, and of transverse coherence effects i.e. violation of the assumption of perfect spoiling in SPGR/FLASH acquisitions (Preibisch and Deichmann, 2009; Yarnykh, 2010). Better agreement between the methods will help establish normative MR parameter values for healthy and diseased brain tissue, establishing qMRI measures as clinical biomarkers. The development of methods for quality assurance on the model of the now well-accepted standards for fMRI (Friedman and Glover, 2006) will improve the

sensitivity of qMRI in multi-center studies (Levesque et al., 2011; Venkatesan et al., 1998).

The ultimate goal of quantitative mapping is to provide surrogate markers for microscopic tissue properties e.g. iron and myelin concentration. Because MR parameters are a mixed effect of multiple tissue properties (Gelman et al., 2001; Rooney et al., 2007), a complete insight into tissue micro-architecture requires quantification of multiple MR parameters. The Multi-Parameter Mapping (MPM) scanning protocol suggested by Helms et al. (2008a,b) allows for 1 mm$^3$ resolution whole-brain mapping of Magnetization Transfer saturation (MT), R1, Proton Density (PD) and R2* in a scan time of ~25 min. With this highly efficient approach, the acquisition parameters are optimized to maximize SNR and minimize bias (Helms and Dechent, 2009; Helms et al., 2011). MPM acquisitions offer interesting prospects for the multivariate study of the brain's morphology (Helms et al., 2009; Lambert et al., 2012) and micro-architecture (Draganski et al., 2011). They were also successfully employed in multi-center studies, significantly improving the comparability of data across sites even at 3 T where inter-site biases are usually more pronounced (Weiskopf et al., in press). Real-time prospective correction of subject motion might prove to be a powerful technological advance to enable ultra-high image resolution in-vivo (Maclaren et al., 2011), correcting for even subtle head motion due to the cardiac pulse.

## Image processing

*Adapting existing processing pipelines to better but different input data*

As cortical surface reconstruction processing pipelines have been made more robust, they have at the same time become more sensitive to and reliant upon the exact statistics of typical T1-weighted input images. Thus, even though quantitative R1 maps are intrinsically preferable to T1-weighted images because the image intensity at each voxel is much more closely correlated with underlying tissue properties, they are more difficult to reconstruct using a pipeline highly optimized for T1-weighted images. This will require re-optimizing those pipelines to use the new images.

One example concerns the skull. In T1-weighted images, the ultra-short relaxation time of bone results in no signal and a harmless almost-black pixel value. Segmentation algorithms in turn rely on this characteristic. Quantitative R1 maps, by contrast, do a poor job of estimating R1 given the small skull signal, which results in increased noise in the skull, which break skull-finding algorithms. Another example is that of the dura between inferotemporal cortex and the cerebellum. The dura has the same R1 value as the cerebellar and cerebral cortices but a higher R2* which leads to dark signal in T1-weighted images. When only R1 maps are used, dura and tissue cannot be distinguished and the reconstructed pial surface shows a tendency to bulge into the dura. Optimization of the surface reconstruction pipeline for qMRI data will require additional procedures such as using multiple quantitative volumes to create a synthetic volume with contrast that is optimized for tissue segmentation (e.g., Fischl et al., 2004).

Another example concerns the impact of small errors in cortical surface reconstruction, which directly influence the accuracy of sampling values at different cortical depths. As can be observed in Fig. 2, the magnitude of the inter-ROI difference in R1 at a given cortical depth was often equal to or less than the R1 difference observed at adjacent cortical depths within the same ROI. For instance, there is a greater difference in R1 values across cortical depths of 0.5 and 0.6 in probabilistically defined MT ('high-MT' in Fig. 2) compared to the difference in R1 between MT and the lightly myelinated angular gyrus when sampled at the same cortical depth (0.5 or 0.6). These findings make it clear that small errors in cortical surface reconstruction (and thereby inaccurate estimates of cortical depth fraction) can decrease sensitivity and precision when mapping myelination, which in turn can affect the assignment of areal borders.
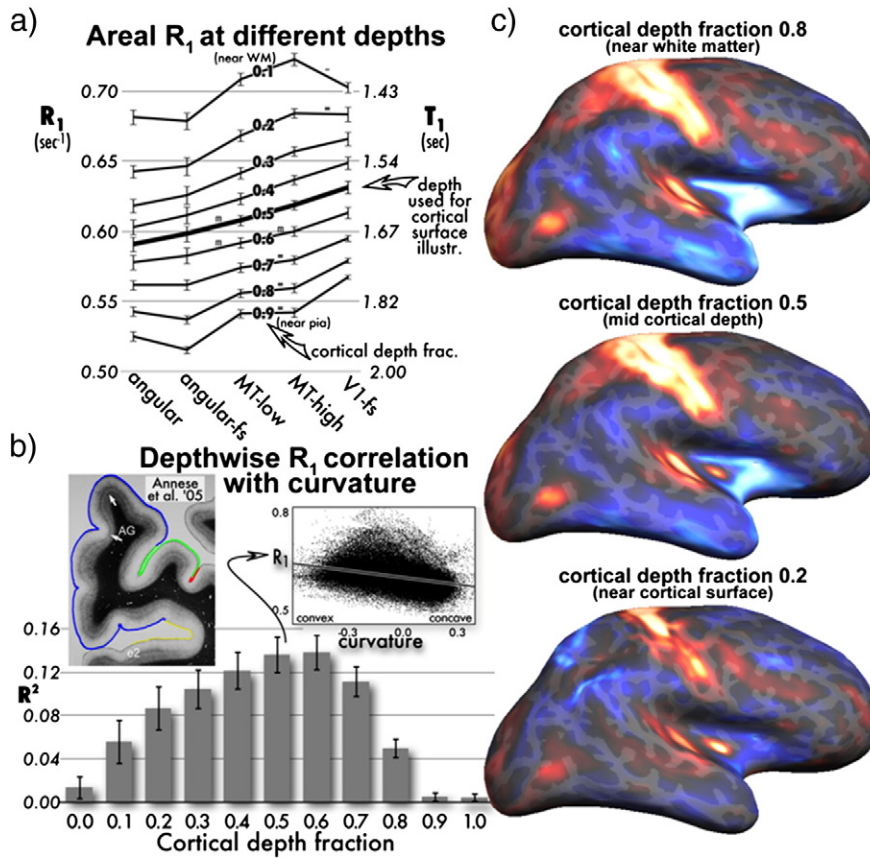
**Fig. 2.** Relaxation rate (R1) as function of cortical depth, area, and curvature. Top left: cross-ROI differences in average cortical R1 shown as line for 8 depths (from 0.1 near white matter to 0.9 near pia); y-axes, error bars show standard error across subjects; ROIs: angular (angular gyrus), angular-fs (Freesurfer angular gyrus label), MT-low and MT-high (non-overlapping low and high probability MT labels (REFS), V1-fs (Freesurfer V1)). All matched-paired t-tests on hypothesized differences significant (p < 0.05) except where marked "m" (p < 0.1), " = " (no significant difference), or "-" (difference opposite prediction). Bottom left: vertex-wise correlation (adjusted $R^2$) of R1 and curvature as function of depth (error bars as before over subjects). Scatter plot inset at right is from a single subject at depth 0.5. For comparison, left inset shows myelin stained section of human cortex with reduced myelination in concave areas (from Annese et al., 2004). Right panel: average 'decurved' R1 values, sampled at three different cortical depth fractions.

Since the improved signal-to-noise of our new methods allows us to generate datasets with voxel sizes less than 1 mm³, we have begun to investigate using higher resolution surface tessellations. Current surface reconstruction pipelines (e.g., Freesurfer) typically begin by resampling data to 1 mm³. Since the resolution of the initial tessellation is based on the square faces of voxels classified as white matter, this generates a standard mesh density that later processing steps (surface refinement, morphing) can rely on.

However, there are advantages to a denser mesh. For example, the additional degrees of freedom afforded by a denser mesh allow more accurate subvoxel estimation of the position of cortical surface boundaries. Fig. 3 compares the result of generating a surface reconstruction after resampling our original (0.8)³ mm³ data to 1 mm³ versus a surface reconstruction after resampling the same data to (0.5)³ mm³. In the first case (left) the gray–white matter surface (rh.white) was reconstructed using the standard Freesurfer pipeline (version 5.1 running on Mac OS X 10.6). In the second case, a surface was reconstructed more simply using only the anisotropic Freesurfer filter and a hard white matter threshold with no normalization of any kind. It is apparent that the fine details of gyral ridges are more accurately rendered by the denser tessellation. The denser tessellation, which contains approximately eight times as many vertices, can be manipulated (inflated, morphed) as before using existing Freesurfer programs (e.g., mris_inflate, mris_sphere, mris_register) after minor adjustments to parameters. These techniques have the potential to improve quantitative R1-based cortical parcellation by minimizing noise in estimating cortical depth.

*Cortical myelination and cortical curvature*

One additional challenge in assessing areal differences in relative myelination is to control for the finding from the post-mortem literature that myeloarchitecture varies significantly with local cortical convexity (Annese et al., 2004). On gyri, as the cortex becomes more convex, the more superficial layers of the cortex puff up and become more myelinated. In sulci, by contrast, the deeper layers thin and all layers become less myelinated. In a sheet of tissue detached from the white matter, one might expect superficial layers on a gyrus to behave similarly to deep layers in a sulcus, since both would be expected to stretch as a sheet of finite thickness was bent. The deeper layers, however, are attached to a mass of white matter, and this may help to explain their substantial asymmetry, which is visible even within a single cortical area. Correspondingly, we found that R1 values were quite strongly related to local cortical curvature, even when cortical thickness was taken into account (Fig. 2b). This relationship was most notable at middle cortical depths – accounting for ~13% of variance – but the correlation extended through much of the depth of cortex (as it does in the Gallyas-stained section included in the figure). Since cortical depth fraction does not account for variation in relative thickness of cortical laminae, however, we cannot exclude the possibility that a portion of this correlation is due to changes in the relative thickness of laminae to compensate cortical folding (Bok, 1929; Waehnert et al., 2014).

Because curvature-associated modulations of R1 can obscure or distort true areal differences in myelination (Annese et al., 2004), we have used curvature- and thickness-residualized maps of R1 variation (latter
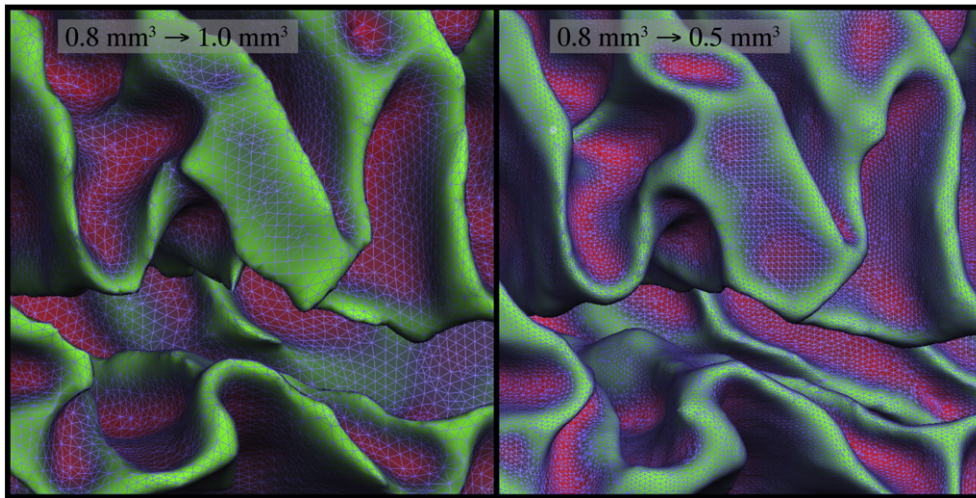
**Fig. 3.** Reconstructed white matter surface from resampled 0.8 mm$^3$ R1 volume, close-up view centered around Sylvian fissure, with mesh showing surface vertices and faces. Left panel shows default Freesurfer reconstruction (Freesurfer version 5.1 on OSX 10.6) from a volume downsampled in resolution from 0.8 mm$^3$ to 1 mm$^3$. Right panel shows the same volume resampled to 0.5 mm$^3$ and reconstructed using only the anisotropic Freesurfer filter and a hard white matter threshold with no normalization of any kind.

called 'decurved/dethickened R1') as a means of improving the visualization of different cortical areas. For example, around area MT, artifactual hyperintensities in the highly curved cortex around this area protruded posteriorly from MT proper along gyral crowns before the dataset was 'decurved'. The inclusion of curvature and thickness in R1 estimates of cortical areas will likely be important for comparisons between primates with highly convoluted brains (humans, chimpanzees) and relatively smooth brains (macaques, owl monkeys).

## Applications

### Cortical myelination and visual areas

Our first study compared R1 maps and retinotopic maps in visual cortex using surface-based methods (Sereno et al., in press). As an initial verification of the technique, we measured six participants' averaged R1 values (sampled at 8 depths in each area) in three probabilistically-
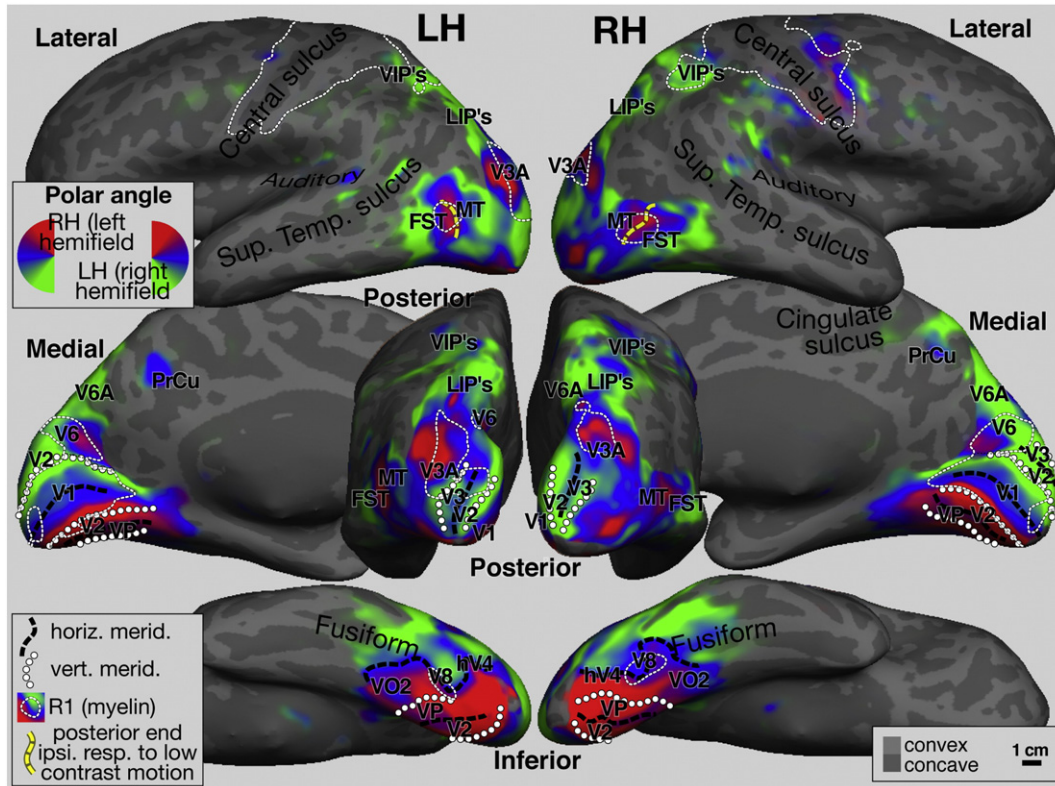


**Fig. 4.** Cross-subject surface average retinotopic maps. Spherical morph average polar angle maps are projected back to the inflated right and left hemispheres of one subject, and shown in lateral (top), posterior (middle-center), medial (middle-sides), and inferior (bottom) views. The posterior boundary of ipsilateral visual responses in MT + is marked by a thick yellow dashed line. Thin dotted lines indicate the boundaries of regions with high quantitative R1 values traced from myelin maps. Vertical and horizontal meridians traced from field sign calculations (not shown) are shown as lines of small circles and thick black dashes. Generalized visual and multisensory area names (V1, V2, V3, VP/V3v, V6, V6A, V8/VO1, V3A, MT/V5, FST, LIP (multiple), VIP (multiple), PrCu [pre-cuneus visual area]) were drawn judiciously from the existing conflicting literature.

defined regions-of-interest (ROIs) known to differ in myelination density — namely the angular gyrus, which is lightly myelinated, and visual areas MT and V1, which are highly myelinated (see Fig. 2a).

First, we found that not only R1 differed across regions (with R1 in the angular gyrus < MT < V1 as expected given postmortem studies), but R1 values within an ROI were also remarkably consistent across subjects at a given cortical depth, as demonstrated by the small standard error bars in Fig. 2a. This suggests that it should be possible to establish areal R1 norms for healthy subjects — ones that could be used as benchmarks for studies of individual differences as well as for early detection of demyelinating diseases such as multiple sclerosis.

Second, we found that the borders of a number of visual areas – as established by retinotopic mapping of polar angle – were associated with changes in R1 values measured in the same individuals (Fig. 4). Cortical boundaries are visible in individuals as well as in cross subject average polar angle maps based on spherical morphing driven by alignment of major sulci. Cross-subject averages not only are smoother, but they also somewhat overemphasize polar angles near the average polar angle (approximately the horizontal meridian, indicated in blue). This is the natural result of a local vector average of slightly displaced, slightly differently sized visual areas containing polar angles ranging from the upper vertical meridian to the lower vertical meridian.

Third, and perhaps our most unexpected finding was centered on the heavily myelinated oval in lateral occipital cortex (see Fig. 4). Although a similarly located region has previously been identified as MT/V5 in a number of studies, our retinotopic mapping data – including both polar angle mapping as well as the location of the posterior boundary of ipsilateral responses in a localizer task (Huk et al., 2002) – showed that MT proper only accounted for the posterior 1/3 to 1/2 of that oval. Previous in-vivo and postmortem studies in humans thus may have substantially overestimated the extent of MT. Given that there are several areas with above average myelination anterior and inferior to MT in monkeys (MST and FST — e.g. Bock et al., 2009), this observation is not completely unexpected. However, the relatively small fraction of this maximum identifiable as MT suggests that those other areas may be relatively larger in humans, or may contain additional subdivisions.
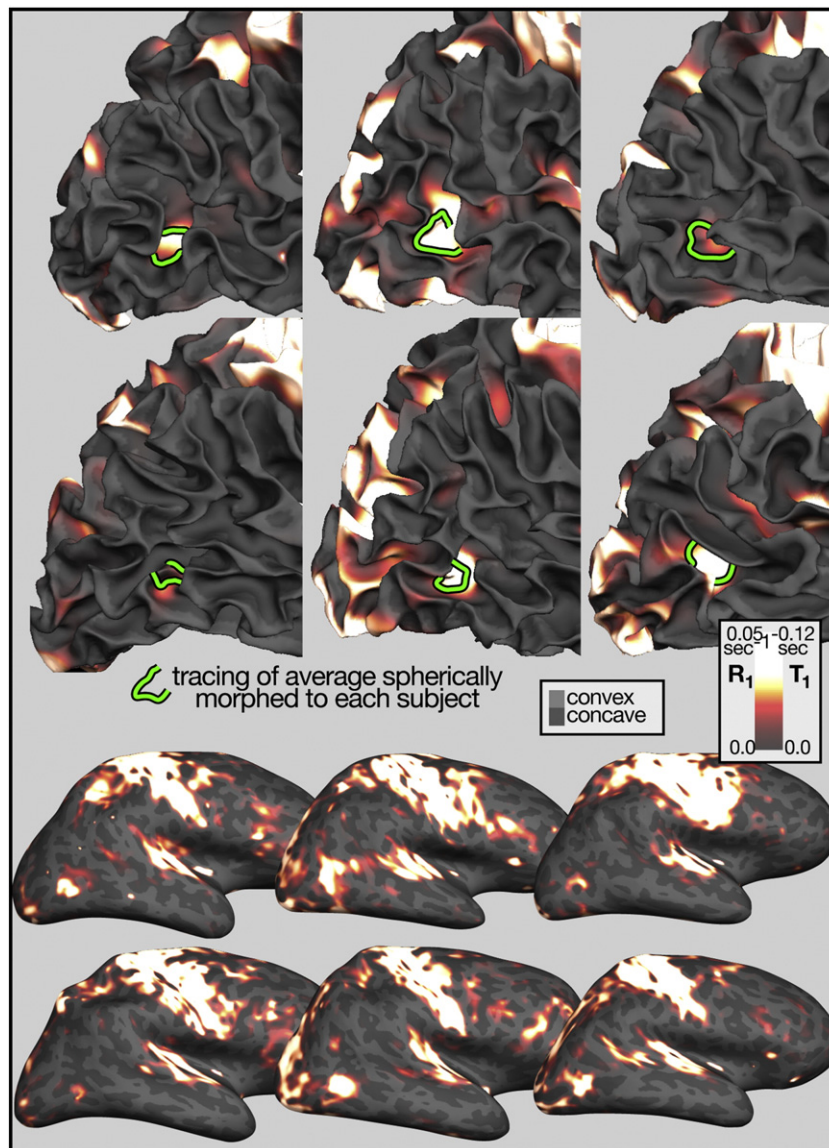


**Fig. 5.** Top two rows: myelin maps from 6 subjects, projected on their reconstructed smooth white matter surface. Average MT+ (calculated on the morphed sphere) is been resampled back to each subject and traced with a green contour. Bottom two rows: the same R1 data from each subject are projected onto the individual's inflated surface at a lower magnification (corresponding placement). In all cases, the data has been rendered using the same mapping between absolute R1 value and color (see inset) and no individual normalization of any kind has been applied.

Finally, though the robust signal visible in the cross subject average demonstrates that different subjects resemble each other, there was considerable cross-subject variation in the regional distribution of R1 hyperintensities, even within our group of 6 healthy adults. This variation can be demonstrated using MT + as an example. The top two rows of Fig. 5 display each subject's myelin map on their reconstructed smooth white matter surface. To see how the average relates to individual subjects, the average MT + (calculated on the morphed sphere) has been resampled back to each subject and traced with a green contour. While a sulcal R1 hyperintensity is observed in every subject, and while it is situated within the average MT + contour in 5 of 6 subjects, — there are clear individual differences in the extent, shape, and positioning of the MT + myelin patch. The same individual subject data is shown in the bottom two rows of Fig. 5 on the inflated surface at a lower magnification (corresponding placement). In all cases, the data have been rendered using the same mapping between absolute R1 value and color (see inset) and no individual normalization of any kind has been applied.

It is critical to be able to visualize this individual variation – akin to what has been observed in postmortem studies of MT and surrounding areas in both human and non-human primates – particularly since immediately adjoining areas may have quite different functional properties. For example, the area directly adjoining MT posteriorly in non-human primates (variously named the MT crescent, MTc, or the V4 transitional area, V4t) is not directionally selective; this stands in striking contrast to strongly directionally selective MT (Baker et al., 1981). However the R1 maps show some variability across repeated scans on the same subjects (Sereno et al., in press). A systematic assessment of the reproducibility of the data will be necessary in order to get a clear picture of the sensitivity of the method to individual differences.

### Myelination in auditory areas

In-vivo myeloarchitectonic assays are of particular importance for auditory neuroscience, in that even the borders of primary auditory areas A1 and R cannot be straightforwardly delineated using functional mapping, particularly using fMRI. Both A1 and R reside in the 'auditory core' (Hackett, 2011), a keyhole-shaped patch of highly myelinated cortex that lies within the medial part of the transverse temporal gyrus and sulcus (Hackett et al., 2001; Sweet et al., 2005; Wallace et al., 2002). Using R1-derived myelin mapping techniques, we were able to identify auditory core both in a spherically-based group average as well as in individual subjects (see Fig. 6). The keyhole shape (viewable on the inflated surfaces of two individual subjects, Fig. 6e), location (medial Heschl's gyrus), and size (on average ~1.9 cm long × ~0.7 cm wide) accord well with reports from the postmortem literature (Wallace et al., 2002), as does the medial-to-lateral decrease in R1 (more visible in the contour lines in Fig. 7). These characteristics were very consistent across scans (see cross-subject scan–rescan comparison — Fig. 6).

By using as regions of interest the Morosan et al. (2001) probabilistic maps of auditory core (their TE1.0) and adjacent regions (TE1.1, 1.2), we were able to show good correspondence with postmortem data, both in terms of overall differences (with myelination in probabilistic TE1.0 considerably higher than in the abutting regions), and in the change in myelin over cortical depth fraction (Fig. 6c). Here, auditory core (TE1.0) shows a more steplike profile of myelination than TE1.1/1.2, with the greatest interareal difference appearing at middle cortical depths, as would be expected. However, we were not able to resolve the very fine structure of the myelin profile in auditory core, e.g., the thin but distinct outer layer of Baillarger and superficial stria
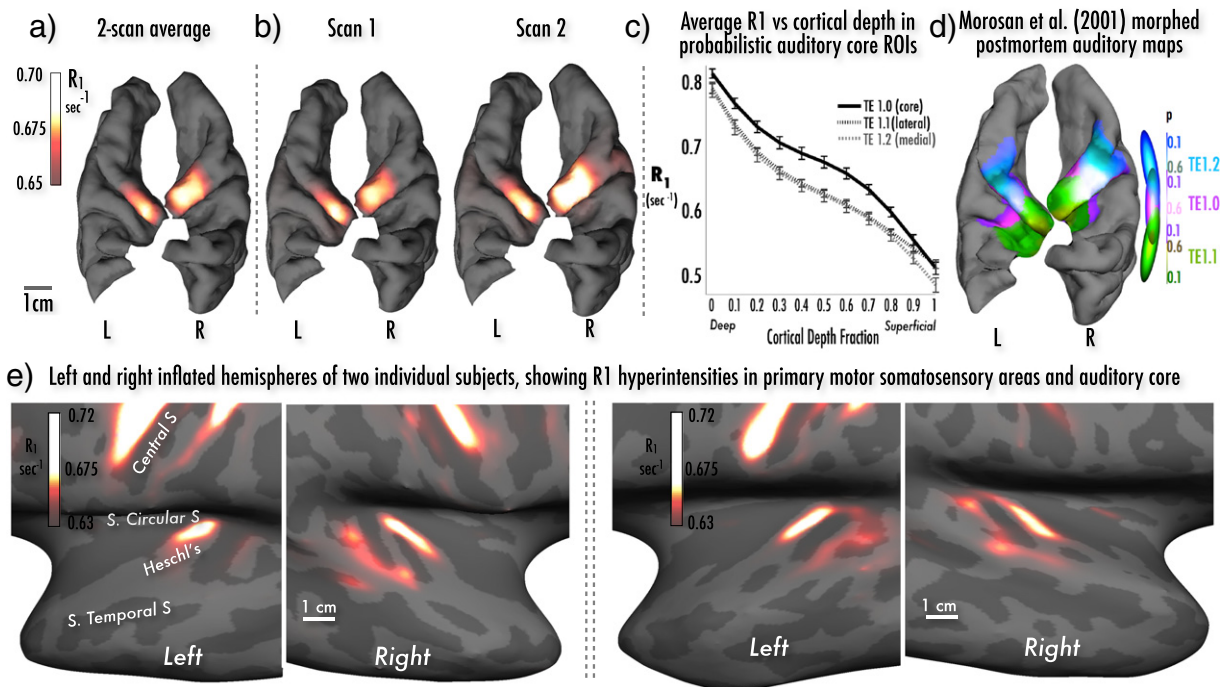


**Fig. 6.** Group average R1 values from 50% of cortical depth, projected onto the pial surface of the digitally resected temporal lobes of a single subject; (a) local increases in R1 values along medial Heschl's gyrus, averaged across both scans (b) single-scan R1 averages show excellent scan–rescan reproducibility; (c) relaxation rate (R1 sec-1) as function of cortical depth, averaged within probabilistically defined subdivisions of Brodmann's area 41 (TE1.0, TE1.1, & TE1.2 according to Morosan et al., 2001). Average R1 within TE1.0 (putative auditory core) decreases steeply from the gray/white boundary (depth fraction 0.0) to a tilted plateau at middle depths (0.3 to 0.6), then again drops steeply at superficial depths (0.7 to 1.0) (error bars: ±1 SEM over subjects). R1 within lateral (TE1.1) and medial (TE1.2) subdivisions shows a more gentle monotonic decrease from deep to superficial cortex. (d) probability maps of cytoarchitectonically defined TE1.0 ('core'), TE1.1, and TE1.2 derived from Morosan et al. (2001). Note that the overlap between probability distributions for TE1.0/TE1.1 and TE1.0/TE1.2 causes some probability maxima for TE1.1 (medial) and TE1.2 (lateral) to be darker colored, as shown in the overlapping probability ovoids at right. (e) Auditory core in the left and right hemispheres of two individual subjects. Each individual's R1 values (shown in heat scale, see scale bar) were sampled at 50% of cortical depth and projected onto the subject's left and right inflated hemispheric surfaces. The auditory core is visible in both hemispheres as a keyhole-shaped hyperintensity maximum running posteromedially to anterolaterally over the medial half of Heschl's gyrus. Hyperintensity maxima can also be observed within the densely myelinated pre- and post-central gyri.

of Kaes–Bechterew (Braitenberg, 1962). As with the visual areas, there was tight clustering of R1 values within each ROI and each cortical sampling depth, suggesting that such quantitative measurements of auditory core might be useable as a normative dataset for diagnostic purposes (for instance, in chronic tinnitus).

Finally, we found very consistent mapping between the location of auditory core and tonotopic progressions (collected from the same subjects). Macaque studies combining in-vivo electrophysiology and post-mortem histology studies of macaque (e.g., (Morel et al., 1993) see Fig. 7,) show a characteristic (but not invariant!) tonotopic progression within core, with highest preferred frequencies observed around the posterior and posteromedial edge of core, then showing a steep high-to-low gradient of preferred frequency moving laterally, ending in a anterolateral low-frequency 'trough'. There is then a gentler, low-to-medium frequency ascent moving anteromedially.

We observed a very similar relationship between tonotopic progression and myeloarchitectonically-defined core in our human subjects. Fig. 7 shows the cortical surface of an individual subject scanned using two different tonotopy protocols, one using bandpass-swept vocalization stimuli (1.5 T, 32-channel head coil; Dick et al. (2012)) and the other using bandpass-swept musical stimuli (7 T, 32-channel head coil). The same 'decurved/dethickened' R1 contours are overlaid on the two maps, with higher R1 values shown in lighter colors; we consider the approximate border of core to be the outer black dashed line. As with the macaque, core is capped posteriorly and posteromedially by regions of high preferred frequency, which (moving anterolaterally) descend to a lateral low-frequency trough; a gentle rise is observed moving anteromedially from the trough to the most anterior part of core.

## Conclusion

Recent in-vivo histological studies using quantitative MRI have demonstrated the validity of the MR parameter R1 as a biomarker for myelin concentration. The subtle changes in R1 across the cortical surface require specially-dedicated MR pulse sequences that allow for accurate, precise and efficient image acquisition with sufficient image resolution to resolve the laminar distribution of the cortical layer. We demonstrated that high-resolution R1 mapping could be used for the in-vivo delineation of multiple cortical areas at 3 T.

MR-based measures of cortical myelination hold great promise not only for basic neuroscience but also for clinical assessment as normative R1 values can be obtained for healthy and diseased tissue. Cortical myelination is often used as a measure in studies of non-human animals, particularly in recent studies of learning and plasticity (Liu et al., 2012). Cross-species comparisons of cortical myelination would be greatly facilitated by high-resolution R1 mapping. Cortical myelination is likely to be directly related to well-characterized biological processes in development and disease progression.

While whole-brain quantitative MR cannot come close to approaching the spatial resolution typical of histological postmortem studies of stained tissue, one advantage over traditional myelin staining, is that one can quantify and map myelin values in an objective way that is not subject to the vagaries of silver impregnation of individual tissue sections. In addition, it is easier to acquire much larger numbers of subjects with MR than is possible with invasive studies in non-human animals, enabling the study of small effects and population variance. Finally multiple datasets can be acquired in the same

R1 contour on inflated right hemisphere shows consistent relationship to cross-site tonotopic mapping in single subject.
Left, tonotopy with filtered vocalization stimulus (1.5T); Right, tonotopic with filtered music stimulus (7T); identical vertices shown in cyan.
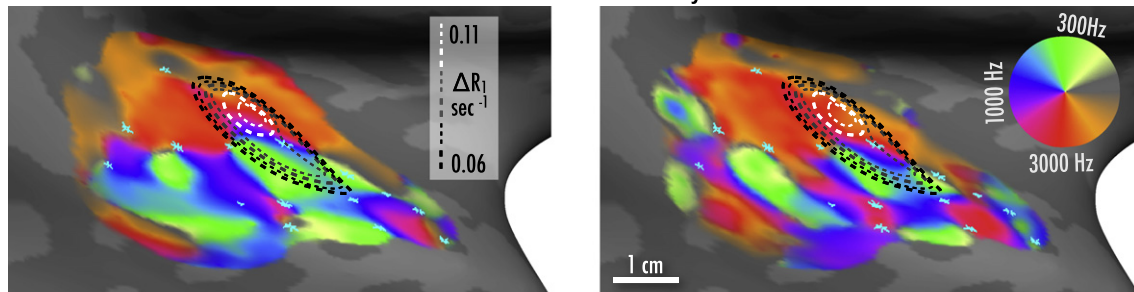
Below: Tonotopic contours across architectonically-defined auditory core in macaque.
Maps redrawn and rendered with data from Figure 2a of Morel, Garraghty, & Kaas (1993)
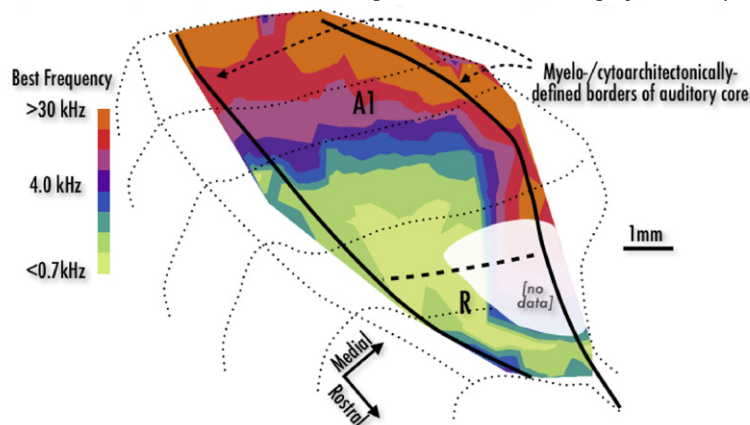
**Fig. 7.** Top Panels: tonotopic maps from an individual subject scanned with different stimuli and on different magnets. Colormap shows characteristic frequency with logarithmic scaling in Hz around the color wheel. Dashed lines show R1 values in grayscale-coded steps of $0.005\ s^{-1}$, with the outermost black line likely to represent the boundaries of auditory core. Tonotopic maps were identically masked using an independent auditory localizer (see Dick et al., 2012 for details). Bottom Panels: analogous recolored physiological recording data from macaque, overlaid with contour of myelo- and cyto-architectonically defined core. Log-frequency isocontours within and around myelo- and cytoarchitectonically-defined auditory core (thick black lines), reconstructed from electrophysiological recording data reported in Fig. 2A of Morel et al. (1993). Thin dotted lines show shape of underlying coronal sections of exposed temporal plane and superior temporal gyrus; thick dashed line is estimate of A1/R border. Fig. 2A from Morel et al. was chosen for having the most extensive set of recording data over A1 and R, and for being representative of other datasets in Morel et al. and in other combined physiology/cytoarchitectonic experiments.

subject over time. Quantitative R1 mapping for myelin is likely to provide new insights into individual differences, their functional/behavioral consequences, and the consistency of mapping between functionally and structurally defined areas.

## Conflict of Interest

The authors declare no conflict of interest.

## References

Akoka, S., Franconi, F., Seguin, F., Lepape, A., 1993. Radiofrequency map of an NMR coil by imaging. Magn. Reson. Imaging 11, 437–441.

Annese, J., Pitiot, A., Dinov, I.D., Toga, A.W., 2004. A myelo-architectonic method for the structural classification of cortical areas. NeuroImage 21, 15–26.

Baker, J.F., Petersen, S.E., Newsome, W.T., Allman, J.M., 1981. Visual response properties of neurons in four extrastriate visual areas of the owl monkey (Aotus trivirgatus): a quantitative comparison of medial, dorsomedial, dorsolateral, and middle temporal areas. J. Neurophysiol. 45, 397–416.

Barazany, D., Assaf, Y., 2012. Visualization of cortical lamination patterns with magnetic resonance imaging. Cereb. Cortex 22, 2016–2023.

Bock, N.A., Kocharyan, A., Liu, J.V., Silva, A.C., 2009. Visualizing the entire cortical myelination pattern in marmosets with magnetic resonance imaging. J. Neurosci. Methods 185, 15–22.

Bock, N.A., Hashim, E., Janik, R., Konyer, N.B., Weiss, M., Stanisz, G.J., Turner, R., Geyer, S., 2013. Optimizing T1-weighted imaging of cortical myelin content at 3.0 T. NeuroImage 65, 1–12.

Bok, S., 1929. Der Einfluß der in den Furchen und Windungen auftretenden Krümmungen der Großhirnrinde auf die Rindenarchitektur. Z. Gesamte Neurol. Psychiatr. 12, 682–750.

Braitenberg, V., 1962. A note on myeloarchitectonics. J. Comp. Neurol. 118, 141–156.

Bridge, H., Clare, S., Krug, K., 2014. Delineating extrastriate visual area MT(V5) using cortical myeloarchitecture. NeuroImage 93, 231–236.

Chavez, S., Stanisz, G.J., 2012. A novel method for simultaneous 3D B1 and T1 mapping: the method of slopes (MoS). NMR Biomed. 25, 1043–1055.

Cheng, H.L., Wright, G.A., 2006. Rapid high-resolution T(1) mapping by variable flip angles: accurate and precise measurements in the presence of radiofrequency field inhomogeneity. Magn. Reson. Med. 55, 566–574.

Chung, S., Kim, D., Breton, E., Axel, L., 2010. Rapid B1+ mapping using a preconditioning RF pulse with TurboFLASH readout. Magn. Reson. Med. 64, 439–446.

Clare, S., Jezzard, P., 2001. Rapid T(1) mapping using multislice echo planar imaging. Magn. Reson. Med. 45, 630–634.

Clark, V.P., Courchesne, E., Grafe, M., 1992. In vivo myeloarchitectonic analysis of human striate and extrastriate cortex using magnetic resonance imaging. Cereb. Cortex 2, 417–424.

Clarke, S., Miklossy, J., 1990. Occipital cortex in man: organization of callosal connections, related myelo- and cytoarchitecture, and putative boundaries of functional visual areas. J. Comp. Neurol. 298, 188–214.

Cunningham, C.H., Pauly, J.M., Nayak, K.S., 2006. Saturated double-angle method for rapid B-1 plus mapping. Magn. Reson. Med. 55, 1326–1333.

Dale, A.M., Fischl, B., Sereno, M.I., 1999. Cortical surface-based analysis. I. Segmentation and surface reconstruction. NeuroImage 9, 179–194.

Deichmann, R., 2005. Fast high-resolution T1 mapping of the human brain. Magn. Reson. Med. 54, 20–27.

Deichmann, R., Haase, A., 1992. Quantification of T1 values by snapshot-FLASH NMR imaging. J. Magn. Reson. Med. 96, 608–612.

Deichmann, R., Hahn, D., Haase, A., 1999. Fast T1 mapping on a whole-body scanner. Magn. Reson. Med. 42, 206–209.

Deoni, S.C., 2007. High-resolution T1 mapping of the brain at 3 T with driven equilibrium single pulse observation of T1 with high-speed incorporation of RF field inhomogeneities (DESPOT1-HIFI). J. Magn. Reson. Imaging 26, 1106–1111.

Deoni, S.C.L., Rutt, B.K., Peters, T.M., 2003. Rapid combined T-1 and T-2 mapping using gradient recalled acquisition in the steady state. Magn. Reson. Med. 49, 515–526.

Deoni, S.C.L., Peters, T.M., Rutt, B.K., 2005. High-resolution T-1 and T-2 mapping of the brain in a clinically acceptable time with DESPOT1 and DESPOT2. Magn. Reson. Med. 53, 237–241.

Dick, F., Taylor, T.A., Lutti, A., Josephs, O., Sereno, M.I., Weiskopf, N., 2012. In vivo functional and myeloarchitectonic mapping of human primary auditory areas. J. Neurosci. 32, 16095–16105.

Draganski, B., Ashburner, J., Hutton, C., Kherif, F., Frackowiak, R.S., Helms, G., Weiskopf, N., 2011. Regional specificity of MRI contrast parameter changes in normal ageing revealed by voxel-based quantification (VBQ). NeuroImage 55, 1423–1434.

Eggenschwiler, F., Kober, T., Magill, A.W., Gruetter, R., Marques, J.P., 2012. SA2RAGE: a new sequence for fast B1+ mapping. Magn. Reson. Med. 67, 1609–1619.

Eickhoff, S.B., Stephan, K.E., Mohlberg, H., Grefkes, C., Fink, G.R., Amunts, K., Zilles, K., 2005. A new SPM toolbox for combining probabilistic cytoarchitectonic maps and functional imaging data. NeuroImage 25, 1325–1335.

Ethofer, T., Mader, I., Seeger, U., Helms, G., Erb, M., Grodd, W., Ludolph, A., Klose, U., 2003. Comparison of longitudinal metabolite relaxation times in different regions of the human brain at 1.5 and 3 Tesla. Magn. Reson. Med. 50, 1296–1301.

Fischl, B., Sereno, M.I., Tootell, R.B., Dale, A.M., 1999. High-resolution intersubject averaging and a coordinate system for the cortical surface. Hum. Brain Mapp. 8, 272–284.

Fischl, B., Salat, D., van der Kouwe, A., Makris, N., Ségonne, F., Quinn, B., Dale, A.M., 2004. Sequence-independent segmentation of magnetic resonance images. NeuroImage 23, S69–S84.

Flechsig, P., 1920. Anatomies des menschlichen Gehirns und Rückenmarks auf myelogenetischer Grundlage. Georg Thieme, Leipzig.

Fleysher, R., Fleysher, L., Liu, S., Gonen, O., 2008. TriTone: a radiofrequency field (B1)-insensitive T1 estimator for MRI at high magnetic fields. Magn. Reson. Imaging 26, 781–789.

Fleysher, R., Fleysher, L., Inglese, M., Sodickson, D., 2011. TROMBONE: T1-relaxation-oblivious mapping of transmit radio-frequency field (B1) for MRI at high magnetic fields. Magn. Reson. Med. 66, 483–491.

Förster, O., 1934. Über die Bedeutung und Reichweite des Lokalisationsprinzips im Nervensystem. Verh. Dtsch. Ges. Inn. Med. 46, 117–211.

Freeman, A.J., Gowland, P.A., Mansfield, P., 1998. Optimisation of the ultra-fast Look–Locker echo-planar imaging T1 mapping sequence. Magn. Reson. Med. 16, 765–772.

Friedman, L., Glover, G.H., 2006. Report on a multicenter fMRI quality assurance protocol. J. Magn. Reson. Imaging 23, 827–839.

Gelman, N., Ewing, J.R., Gorell, J.M., Spickler, E.M., Solomon, E.G., 2001. Interregional variation of longitudinal relaxation rates in human brain at 3.0 T: relation to estimated iron and water contents. Magn. Reson. Med. 45, 71–79.

Geyer, S., Weiss, M., Reimann, K., Lohmann, G., Turner, R., 2011. Microstructural parcellation of the human cerebral cortex — from Brodmann's post-mortem map to in vivo mapping with high-field magnetic resonance imaging. Front. Hum. Neurosci. 18, 5–19.

Glasser, M.F., Van Essen, D.C., 2011. Mapping human cortical areas in vivo based on myelin content as revealed by T1- and T2-weighted MRI. J. Neurosci. 31, 11597–11616.

Glover, G.H., Hayes, C.E., Pelc, N.J., Edelstein, W.A., Mueller, O.M., Hart, H.R., Hardy, C.J., O'Donnell, M., Barber, W.D., 1985. Comparison of linear and circular polarization for magnetic resonance imaging. J. Magn. Reson. 64, 255–270.

Gowland, P.A., Leach, M.O., 1992. Fast and accurate measurements of T1 using a multi-readout single inversion–recovery sequence. Magn. Reson. Med. 26, 79–88.

Gowland, P.A., Mansfield, P., 1993. Accurate measurement of T1 in vivo in less than 3 seconds using echo-planar imaging. Magn. Reson. Med. 30, 351–354.

Graziano, M.S., Aflalo, T.N., 2007. Mapping behavioral repertoire onto the cortex. Neuron 56, 239–251.

Haase, A., 1990. Snapshot FLASH MRI, application to T1, T2, and chemical-shift imaging. Magn. Reson. Med. 13, 77–89.

Haase, A., Frahm, J., Matthaei, D., Hanicke, W., Merboldt, K.D., 1986. Flash imaging — rapid NMR imaging using low flip-angle pulses. J. Magn. Reson. 67, 258–266.

Haase, A., Matthaei, D., Bartkowski, R., Dühmke, E., Leibfritz, D., 1989. Inversion recovery snapshot FLASH MR Imaging. J. Comput. Assist. Tomogr. 13, 1036–1040.

Hackett, T.A., 2011. Information flow in the auditory cortical network. Hear. Res. 271, 133–146.

Hackett, T.A., Preuss, T.M., Kaas, J.H., 2001. Architectonic identification of the core region in auditory cortex of macaques, chimpanzees, and humans. J. Comp. Neurol. 441, 197–222.

Helms, G., Dechent, P., 2009. Increased SNR and reduced distortions by averaging multiple gradient echo signals in 3D FLASH imaging of the human brain at 3 T. J. Magn. Reson. Imaging 29, 198–204.

Helms, G., Dathe, H., Dechent, P., 2008a. Quantitative FLASH MRI at 3 T using a rational approximation of the Ernst equation. Magn. Reson. Med. 59, 667–672.

Helms, G., Dathe, H., Kallenberg, K., Dechent, P., 2008b. High-resolution maps of magnetization transfer with inherent correction for RF inhomogeneity and T1 relaxation obtained from 3D FLASH MRI. Magn. Reson. Med. 60, 1396–1407.

Helms, G., Finsterbusch, J., Weiskopf, N., Dechent, P., 2008c. Rapid radiofrequency field mapping in vivo using single-shot STEAM MRI. Magn. Reson. Med. 60, 739–743.

Helms, G., Draganski, B., Frackowiak, R., Ashburner, J., Weiskopf, N., 2009. Improved segmentation of deep brain grey matter structures using magnetization transfer (MT) parameter maps. NeuroImage 47, 194–198.

Helms, G., Dathe, H., Weiskopf, N., Dechent, P., 2011. Identification of signal bias in the variable flip angle method by linear display of the algebraic Ernst equation. Magn. Reson. Med. 66, 669–677.

Henderson, E., McKinnon, G., Lee, T.Y., Rutt, B.K., 1999. A fast 3D Look–Locker method for volumetric T1 mapping. Magn. Reson. Imaging 17, 1163–1171.

Henkelman, R., Huang, X., Xiang, Q.-S., Stanisz, G., Swanson, G., Bronskill, M., 1993. Quantitative interpretation of magnetization transfer. Magn. Reson. Med. 29, 759–766.

Hinds, O., Polimeni, J.R., Rajendran, N., Balasubramanian, M., Wald, L.L., Augustinack, J.C., Wiggins, G., Rosas, H.D., Fischl, B., Schwartz, E.L., 2008. The intrinsic shape of human and macaque primary visual cortex. Cereb. Cortex 18, 2586–2595.

Homer, J., Beevers, M.S., 1985. Driven-equilibrium single-pulse observation of T1 relaxation — a reevaluation of a rapid new method for determining NMR spin–lattice relaxation-times. J. Magn. Reson. 63, 287–297.

Homer, J., Roberts, J.K., 1987. Conditions for the driven equilibrium single pulse observation of spin–lattice relaxation-times. J. Magn. Reson. 74, 424–432.

Hopf, A., 1951. Die Myeloarchitektonik des Isocortex temporalis beim Menschen. J. Hirnforsch. 2, 208–279.

Hopf, A., 1955. Über die Verteilung myeloarchitektonischer Merkmale in der isokortikalen Schläfenlappenrinde beim Menschen. J. Hirnforsch. 46–54.

Hsu, J.J., Zaharchuk, G., Glover, G.H., 2009. Rapid methods for concurrent measurement of the RF-pulse flip angle and the longitudinal relaxation time. Magn. Reson. Med. 61, 1319–1325.

Huk, A.C., Dougherty, R.F., Heeger, D.J., 2002. Retinotopy and functional subdivision of human areas MT and MST. J. Neurosci. 22, 7195–7205.

Hurley, A.H., Yarnykh, V.L., Johnson, K.M., Field, A.S., Alexander, A.L., Samsonov, A.A., 2012. Simultaneous variable flip angle–actual flip angle imaging method for improved accuracy and precision of three-dimensional T1 and B1 measurements. Magn. Reson. Med. 68, 54–64.

Hutton, C., Bork, A., Josephs, O., Deichmann, R., Ashburner, J., Turner, R., 2002. Image distortion correction in fMRI: a quantitative evaluation. NeuroImage 16, 217–240.

Insko, E.K., Bolinger, L., 1993. Mapping of the radiofrequency field. J. Magn. Reson. A 103, 82–85.

Jankiewicz, M., Gore, J.C., Grissom, W.A., 2013. Improved encoding pulses for Bloch–Siegert B1+ mapping. J. Magn. Reson. 226, 79–87.

Jiru, F., Klose, U., 2006. Fast 3D radiofrequency field mapping using echo-planar imaging. Magn. Reson. Med. 56, 1375–1379.

Karns, C.M., Dow, M.W., Neville, H.J., 2012. Altered cross-modal processing in the primary auditory cortex of congenitally deaf adults: a visual-somatosensory fMRI study with a double-flash illusion. J. Neurosci. 32, 9626–9638.

Koenig, S.H., 1991. Cholesterol of myelin is the determinant of gray–white contrast in MRI of brain. Magn. Reson. Med. 20, 285–291.

Koenig, S.H., Brown III, R.D., Spiller, M., Lundbom, N., 1990. Relaxometry of brain: why white matter appears bright in MRI. Magn. Reson. Med. 14, 482–495.

Lambert, C., Zrinzo, L., Nagy, Z., Lutti, A., Hariz, M., Foltynie, T., Draganski, B., Ashburner, J., Frackowiak, R., 2012. Confirmation of functional zones within the human subthalamic nucleus: patterns of connectivity and sub-parcellation using diffusion weighted imaging. NeuroImage 60, 83–94.

Lee, J.H., 2000. PURR-TURBO: a novel pulse sequence for longitudinal relaxographic imaging. Magn. Reson. Med. 43, 773–777.

Levesque, I.R., Stikov, N., Pike, G.B., Pauly, J.M., 2011. Drift in the magnetization transfer signal: effect on quantitative MT experiments. Proceedings of the 19th Annual Meeting of ISMRM.

Liu, J.V., Bock, N.A., Silva, A.C., 2011. Rapid high-resolution three-dimensional mapping of T1 and age-dependent variations in the non-human primate using magnetization-prepared rapid gradient-echo (MPRAGE) sequence. NeuroImage 56, 1154–1163.

Liu, J., Dietz, K., Deloyht, J.M., Pedre, X., Kelkar, D., Kaur, J., Vialou, V., Lobo, M.K., Dietz, D.M., Nestler, E.J., Dupree, J., Casaccia, P., 2012. Impaired adult myelination in the prefrontal cortex of socially isolated mice. Nat. Neurosci. 15, 1621–1623.

Look, D.C., Locker, D.R., 1970. Time saving in measurement of NMR and EPR relaxation times. Rev. Sci. Instrum. 41, 250–251.

Lutti, A., Hutton, C., Finsterbusch, J., Helms, G., Weiskopf, N., 2010. Optimization and validation of methods for mapping of the radiofrequency transmit field at 3 T. Magn. Reson. Med. 64, 229–238.

Lutti, A., Stadler, J., Josephs, O., Windischberger, C., Speck, O., Bernarding, J., Hutton, C., Weiskopf, N., 2012. Robust and fast whole brain mapping of the RF transmit field B1 at 7 T. PLoS One 7, e32379.

MacKay, A., Laule, C., Vavasour, I., Bjarnason, T., Kolind, S., Madler, B., 2006. Insights into brain microstructure from the T2 distribution. Magn. Reson. Imaging 24, 515–525.

Maclaren, J., Lee, K.J., Luengviriya, C., Speck, O., Zaitsev, M., 2011. Combined prospective and retrospective motion correction to relax navigator requirements. Magn. Reson. Med. 65, 1724–1732.

Marques, J.P., Gruetter, R., 2013. Exploring cortical cytoarchitecture in high resolution R1 maps. Proceedings of the 21st Annual Meeting of ISMRM, p. 266.

Marques, J.P., Kober, T., Krueger, G., van der Zwaag, W., Van de Moortele, P.F., Gruetter, R., 2010. MP2RAGE, a self bias-field corrected sequence for improved segmentation and T1-mapping at high field. NeuroImage 49, 1271–1281.

Morel, A., Garraghty, P.E., Kaas, J.H., 1993. Tonotopic organization, architectonic fields, and connections of auditory cortex in macaque monkeys. J. Comp. Neurol. 335, 437–459.

Morosan, P., Rademacher, J., Schleicher, A., Amunts, K., Schormann, T., Zilles, K., 2001. Human primary auditory cortex: cytoarchitectonic subdivisions and mapping into a spatial reference system. NeuroImage 13, 684–701.

Morrell, G.R., 2008. A phase-sensitive method of flip angle mapping. Magn. Reson. Med. 60, 889–894.

Mottershead, J.P., Schmierer, K., Clemence, M., Thornton, J.S., Scaravilli, F., Barker, G.J., Tofts, P.S., Newcombe, J., Cuzner, M.L., Ordidge, R.J., McDonald, W.I., Miller, D.H., 2003. High field MRI correlates of myelin content and axonal density in multiple sclerosis. J. Neurol. 250, 1293–1301.

Mugler, J.P., Brookeman, J.R., 1990. Three-dimensional magnetization-prepared rapid gradient-echo imaging (3D MP RAGE). Magn. Reson. Med. 15, 152–157.

Nehrke, K., 2009. On the steady-state properties of actual flip angle imaging (AFI). Magn. Reson. Med. 61, 84–92.

Nehrke, K., Börnert, P., 2012. DREAM — a novel approach for robust, ultrafast, multislice B1 mapping. Magn. Reson. Med. 68, 1517–1526.

Ordidge, R.J., Gibbs, P., Chapman, B., Stehling, M.K., Mansfield, P., 1990. High-speed multislice T1 mapping using inversion recovery echo-planar imaging. Magn. Reson. Med. 16, 238–245.

Preibisch, C., Deichmann, R., 2009. Influence of RF spoiling on the stability and accuracy of T1 mapping based on spoiled FLASH with varying flip angles. Magn. Reson. Med. 61, 125–135.

Ressel, V., Pallier, C., Ventura-Campos, N., Diaz, B., Roessler, A., Avila, C., Sebastian-Galles, N., 2012. An effect of bilingualism on the auditory cortex. J. Neurosci. 32, 16597–16601.

Rooney, W.D., Johnson, G., Li, X., Cohen, E.R., Kim, S.G., Ugurbil, K., Springer Jr., C.S., 2007. Magnetic field and tissue dependencies of human brain longitudinal 1H2O relaxation in vivo. Magn. Reson. Med. 57, 308–318.

Sacolick, L.I., Wiesinger, F., Hancu, I., Vogel, M.W., 2010. B1 mapping by Bloch–Siegert shift. Magn. Reson. Med. 63, 1315–1322.

Sánchez-Panchuelo, R.M., Francis, S.T., Schluppeck, D., Bowtell, R.W., 2012. Correspondence of human visual areas identified using functional and anatomical MRI in vivo at 7 T. J. Magn. Reson. Imaging 35, 287–299.

Saygin, A.P., Sereno, M.I., 2008. Retinotopy and attention in human occipital, temporal, parietal, and frontal cortex. Cereb. Cortex 18, 2158–2168.

Schmierer, K., Scaravilli, F., Altmann, D.R., Barker, G.J., Miller, D.H., 2004. Magnetization transfer ratio and myelin in postmortem multiple sclerosis brain. Ann. Neurol. 56, 407–415.

Schmierer, K., Wheeler-Kingshott, C.A.M., Tozer, D.J., Boulby, P.A., Parkes, H.G., Yousry, T.A., Scaravilli, F., Barker, G.J., Tofts, P.S., Miller, D.H., 2008. Quantitative magnetic resonance of postmortem multiple sclerosis brain before and after fixation. Magn. Reson. Med. 59, 268–277.

Schreiner, C.E., Winer, J.A., 2007. Auditory cortex mapmaking: principles, projections, and plasticity. Neuron 56, 356–365.

Schwarzkopf, D.S., Song, C., Rees, G., 2011. The surface area of human V1 predicts the subjective experience of object size. Nat. Neurosci. 14, 28–30.

Sereno, M.I., Tootell, R.B., 2005. From monkeys to humans: what do we now know about brain homologies? Curr. Opin. Neurobiol. 15, 135–144.

Sereno, M.I., Lutti, A., Weiskopf, N., Dick, F. in press. Mapping the human cortical surface by combining quantitative T1 with retinotopy. Cereb. Cortex. http://dx.doi.org/10.1093/cercor/bhs213.

Shah, N.J., Zaitsev, M., Steinhoff, S., Zilles, K., 2001. A new method for fast multislice T(1) mapping. NeuroImage 14, 1175–1185.

Sigalovsky, I.S., Fischl, B., Melcher, J.R., 2006. Mapping an intrinsic MR property of gray matter in auditory cortex of living humans: a possible marker for primary cortex and hemispheric differences. NeuroImage 32, 1524–1537.

Silver, M.A., Kastner, S., 2009. Topographic maps in human frontal and parietal cortex. Trends Cogn. Sci. 13, 488–495.

Sled, J.G., Pike, G.B., 1998. Standing-wave and RF penetration artifacts caused by elliptic geometry: an electrodynamic analysis of MRI. IEEE Trans. Med. Imaging 17, 653–662.

Sled, J.G., Pike, G.B., 2000. Correction for B-1 and B-0 variations in quantitative T-2 measurements using MRI. Magn. Reson. Med. 43, 589–593.

Smith, G.E., 1907. A new topographical survey of the human cerebral cortex, being an account of the distribution of the anatomically distinct cortical areas and their relationship to the cerebral sulci. J. Anat. Physiol. 41, 237.

Steinhoff, S., Zaitsev, M., Zilles, K., Shah, N.J., 2001. Fast T(1) mapping with volume coverage. Magn. Reson. Med. 46, 131–140.

Stollberger, R., Wach, P., 1996. Imaging of the active B-1 field in vivo. Magn. Reson. Med. 35, 246–251.

Sweet, R.A., Dorph-Petersen, K.A., Lewis, D.A., 2005. Mapping auditory core, lateral belt, and parabelt cortices in the human superior temporal gyrus. J. Comp. Neurol. 491, 270–289.

Tahmasebi, A.M., Abolmaesumi, P., Geng, X., Morosan, P., Amunts, K., Christensen, G.E., Johnsrude, I.S., 2009. A new approach for creating customizable cytoarchitectonic probabilistic maps without a template. Med. Image Comput. Comput. Assist. Interv. 12, 795–802.

Tardif, C.L., Waehnert, M., Dinse, J., Schäfer, A., Bazin, P.-L., Turner, R., 2013. High-resolution quantitative T1 maps of the human stria of Gennari at 7 Tesla. Proceedings of the 21st Annual Meeting of ISMRM, p. 267.

Trampel, R., Ott, D.V., Turner, R., 2011. Do the congenitally blind have a stria of Gennari? First intracortical insights in vivo. Cereb. Cortex 21, 2075–2081.

Venkatesan, R., Lin, W.L., Haacke, E.M., 1998. Accurate determination of spin-density and T-1 in the presence of RF-field inhomogeneities and flip-angle miscalibration. Magn. Reson. Med. 40, 592–602.

Vogt, O., 1906. Der Wert der myelogenetischen Felder der Großhirnrinde. Anat. Anz. 24, 273–287.

Voigt, T., Nehrke, K., Doessel, O., Katscher, U., 2010. T1 corrected B1 mapping using multi-TR gradient echo sequences. Magn. Reson. Med. 64, 725–733.

von Economo, C., Koskinas, G., 1925. Die Cytoarchitektonik der Hirnrinde des erwachsenen Menschen. Springer, Berlin.

Waehnert, M.D., Dinse, J., Tardif, C.L., Schäfer, A., Geyer, S., Bazin, P.-L., Turner, R., 2013. How much resolution is needed for in-vivo analysis of cortical myeloarchitecture? Proceedings of the 21st Annual Meeting of ISMRM, p. 270.

Waehnert, M.D., Dinse, J., Weiss, M., Streicher, M.N., Waehnert, P., Geyer, S., Turner, R., Bazin, P.-L., 2014. Anatomically motivated modeling of cortical laminae. NeuroImage 93P2, 210–220.

Wallace, M.N., Johnston, P.W., Palmer, A.R., 2002. Histochemical identification of cortical areas in the auditory region of the human brain. Exp. Brain Res. 143, 499–508.

Walters, N.B., Egan, G.F., Kril, J.J., Kean, M., Waley, P., Jenkinson, M., Watson, J.D., 2003. In vivo identification of human cortical areas using high-resolution MRI: an approach to cerebral structure–function correlation. Proc. Natl. Acad. Sci. U. S. A. 100, 2981–2986.

Wandell, B.A., Dumoulin, S.O., Brewer, A.A., 2007. Visual field maps in human cortex. Neuron 56, 366–383.

Wang, H.Z., Riederer, S.J., Lee, J.N., 1987. Optimizing the precision in T1 relaxation estimation using limited flip angles. Magn. Reson. Med. 5, 399–416.

Wang, J.H., Qiu, M.L., Constable, R.T., 2005. In vivo method for correcting transmit/receive nonuniformities with phased array coils. Magn. Reson. Med. 53, 666–674.

Wansapura, J.P., Holland, S.K., Dunn, R.S., Ball, W.S., 1999. NMR relaxation times in the human brain at 3.0 Tesla. J. Magn. Reson. Imaging 9, 531–538.

Weiskopf, N., Lutti, A., Helms, G., Novak, M., Ashburner, J., Hutton, C., 2011. Unified segmentation based correction of R1 brain maps for RF transmit field inhomogeneities (UNICORT). NeuroImage 54, 2116–2124.

Weiskopf, N., Suckling, J., Williams, G., Correia, M.M., Inkster, B., Tait, R., Ooi, C., Bullmore, E.T., Lutti, A., 2013. Quantitative multi-parameter mapping of R1, PD*, MT and R2* at 3 T: a multi-center validation. [cited 2013 May 20] Front. Neurosci. 7, 95. http://dx.doi.org/10.3389/fnins.2013.00095 ([in press], Available from http://www.frontiersin.org/Brain_Imaging_Methods/10.3389/fnins.2013.00095/abstract).

Weiss, M., Geyer, S., Lohmann, G., Trampel, R., Turner, R., 2011. Quantitative T1 mapping at 7 Tesla identifies primary functional areas in the living human brain. Proceedings of the 19th Annual Meeting of ISMRM, p. 2360.

Wright, P.J., Mougin, O.E., Totman, J.J., Peters, A.M., Brookes, M.J., Coxon, R., Morris, P.E., Clemence, M., Francis, S.T., Bowtell, R.W., Gowland, P.A., 2008. Water proton T-1 measurements in brain tissue at 7, 3, and 1.5 T using IR–EPI, IR–TSE, and MPRAGE: results and optimization. Magn. Reson. Mater. Phys. Biol. Med. 21, 121–130.

Yarnykh, V.L., 2007. Actual flip-angle imaging in the pulsed steady state: a method for rapid three-dimensional mapping of the transmitted radiofrequency field. Magn. Reson. Med. 57, 192–200.

Yarnykh, V.L., 2010. Optimal radiofrequency and gradient spoiling for improved accuracy of T1 and B1 measurements using fast steady-state techniques. Magn. Reson. Med. 63, 1610–1626.

Zhu, D.C., Penn, R.D., 2005. Full-brain T1 mapping through inversion recovery fast spin echo imaging with time-efficient slice ordering. Magn. Reson. Med. 54, 725–731.

Zilles, K., Amunts, K., 2010. Centenary of Brodmann's map—conception and fate. Nat. Rev. Neurosci. 11, 139–145.